Earth and Planetary Science Letters 561 (2021) 116855

Contents lists available at ScienceDirect

Earth and Planetary Science Letters

www.elsevier.com/locate/epsl

China's Chang'e-5 landing site: Geology, stratigraphy, and provenance of materials

Yuqi Qian [a,b], Long Xiao [a,c,*], Qian Wang [d], James W. Head [b,**], Ruihong Yang [d], Yan Kang [d], Carolyn H. van der Bogert [e], Harald Hiesinger [e], Xiaoming Lai [f], Guoxing Wang [f], Yong Pang [f], Nai Zhang [f], Yuefeng Yuan [g], Qi He [a], Jun Huang [a], Jiannan Zhao [a], Jiang Wang [a], Siyuan Zhao [a]

[a] *State Key Laboratory of Geological Processes and Mineral Resources, Planetary Science Institute, School of Earth Sciences, China University of Geosciences, Wuhan, China*
[b] *Department of Earth, Environmental, and Planetary Sciences, Brown University, Providence, USA*
[c] *Center for Excellence in Comparative Planetology, Chinese Academy of Sciences, Hefei, China*
[d] *Lunar Exploration and Space Engineering Center, Beijing, China*
[e] *Institut für Planetologie, Westfälische Wilhelms-Universität Münster, Münster, Germany*
[f] *Beijing Spacecrafts, Beijing, China*
[g] *Institute of Geophysics and Geomatics, China University of Geosciences, Wuhan, China*

ARTICLE INFO

Article history:
Accepted 21 February 2021
Available online xxxx
Editor: W.B. McKinnon

Keywords:
Chang'e-5
landing site
chronology
geological mapping
mare basalts
regolith

ABSTRACT

China's Chang'e-5 (CE-5) mission, the first lunar sample return mission since 1976, landed at 43.06°N, 51.92°W on Dec. 1, 2020, in Northern Oceanus Procellarum. CE-5 targeted a mare plain (Em4/P58) composed of distinctive young (~1.6-1.7 Ga) moderate-Ti mare basalts, with elevated Th abundance (inherent or extraneous). Thus, the regolith and rock fragments sampled by CE-5 come from some of the youngest mare basalts on the Moon, near Rima Sharp, and from the center of the globally anomalous Procellarum KREEP Terrane (PKT), hypothesized to be responsible for the generation of the young volcanism. To provide context for the analysis and interpretation of the returned samples and in-situ measurements of the regolith substructure with penetrating radar, we constructed a detailed geologic map and stratigraphic assessment of the site. The stratigraphy consists of ancient highland materials (PKT crust and ejecta from Iridum and Imbrium basins), local silica-rich volcanism, overlain by a sequence of mare basalts, capped with Em4/P58. A ~4-7 m thick regolith layer developed by post-mare bombardment overlies the Em4/P58 protolith and contains admixed impact ejecta from distant sources, mainly from Harpalus (~6 wt.%), followed by Copernicus (~2 wt.%) and Aristarchus (~1 wt.%). New crater size-frequency measurements of Em4/P58 provide the necessary crater spatial density reference for calibration of the lunar cratering chronology with radiometric ages of the returned samples. The geological map and assessment of regolith provenance indicate that samples returned by CE-5 will address fundamental questions in lunar chronology, thermal evolution, basalt petrogenesis, and the nature of PKT, as well as provide key calibration for lunar and planetary chronologies and remote sensing data.

1. Introduction

Chang'e-5 (CE-5), China's first lunar sample return mission and the first sampling attempt since Luna-24, landed on December 1, 2020 at 43.06°N, 51.92°W (Wang et al., 2021) in Northern Oceanus Procellarum (Fig. 1), ~170 km ENE from Mons Rümker (Zhao et al., 2017). The landing site (Fig. 2) is within some of the youngest lunar mare basalts (1.21 Ga, Qian et al., 2018; 1.33 Ga, Hiesinger et al., 2011; 1.53 Ga, Qian et al., 2021; 1.91 or 2.20 Ga, Morota et al., 2011), representing material not sampled by any previous missions (Tartèse et al., 2019). Based on remote sensing data, the dominant geologic unit at the landing site consists of moderate-Ti (5-8 wt.%), high-Th content (5-8.5 ppm, inherent or extraneous), and relatively high-olivine Eratosthenian-aged mare basalts (~13 wt.%) (Qian et al., 2021, 2018). Moderate-Ti mare basalts have been

---

* Corresponding author at: State Key Laboratory of Geological Processes and Mineral Resources, Planetary Science Institute, School of Earth Sciences, China University of Geosciences, Wuhan, China.
** Corresponding author.
E-mail addresses: longxiao@cug.edu.cn (L. Xiao), James_Head@brown.edu (J.W. Head).

https://doi.org/10.1016/j.epsl.2021.116855
0012-821X/

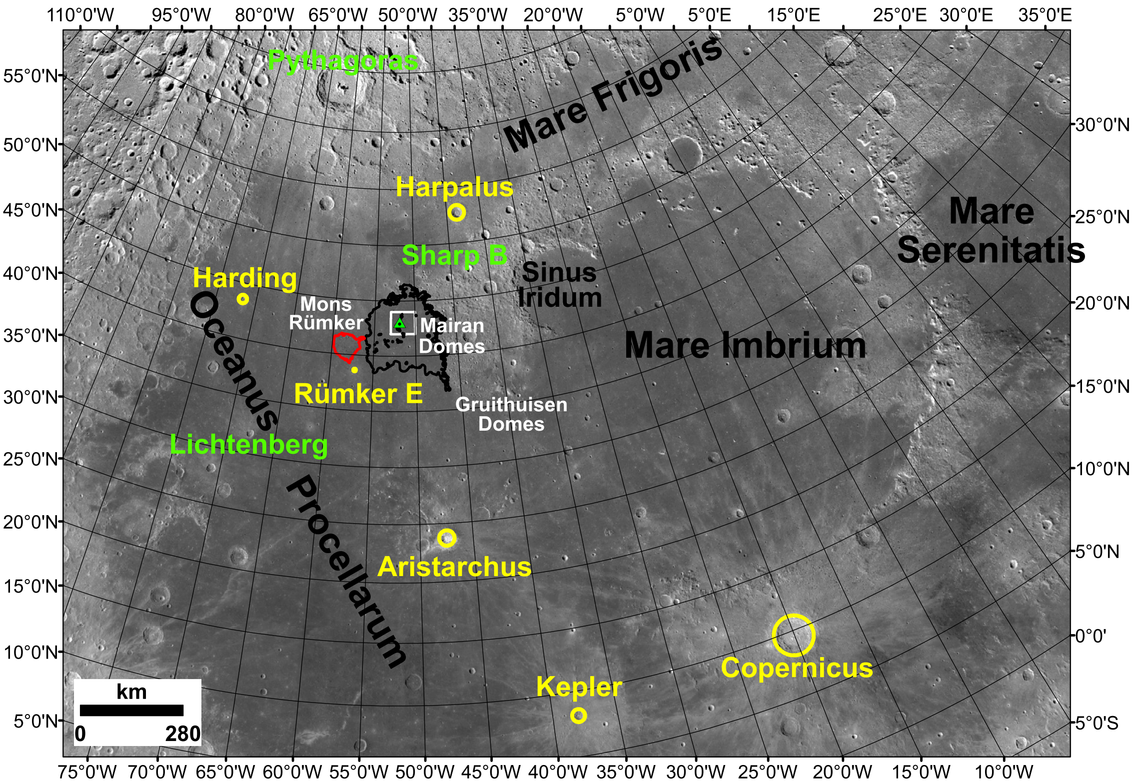

Fig. 1. Regional context of the CE-5 landing site (green triangle) on the Em4/P58 mare basalts (black outline) adjacent to Mons Rümker (red outline). The white box (42-44°N, 40-53°W) shows the area mapped in this study. The craters labeled in green and yellow represent the pre-Em4/P58 and post-Em4/P58 impact craters, respectively. (For interpretation of the colors in the figure(s), the reader is referred to the web version of this article.)

investigated by Chang'e-3 in-situ (Zhao et al., 2014), and collected by the Apollo-16 (Fagan and Neal, 2016) and Apollo-12 missions (Neal et al., 1994), however, the CE-5 landing site is much younger than them. The CE-5 mare basalts, located in the PKT (Jolliff et al., 2000a), have enormous potential for improving our understanding of the recent thermal evolution and impact history of the Moon (National Research Council, 2007; Qian et al., 2021).

Soil and rock fragments returned by CE-5 will be carefully studied in laboratories using cutting-edge techniques (Zhang et al., 2020). An understanding of the provenance of the materials at the CE-5 landing site from a variety of perspectives (temporal, local, regional, global, and with depth below the surface) is essential to address the series of fundamental scientific questions. For the CE-5 landing site, continuous impact and space weathering processes after the emplacement of the mare protolith control the compositions of lunar soils (Head and Wilson, 2020; McKay et al., 1991); and here the underlying moderate-Ti basalts can be used to study the late-stage lunar volcanism (Head and Wilson, 2017; Wilson and Head, 2017). Regolith is developed on top of all geological units on the Moon, following their emplacement, due to the destructive effects of cratering and ejecta emplacement at all scales, in addition to space weatherings (Pieters and Noble, 2016). Thus, it is certain that the CE-5 samples will contain components from different proximal and distal sources, as also shown by Apollo/Luna missions (e.g., McKay et al., 1991). Distal impact ejecta permits the study of distant impact events/materials, which may carry deep crust/mantle components, extending knowledge of the Moon areally and in the subsurface.

Recently, new geological maps for the Apollo-11/12 landing sites (Iqbal et al., 2020, 2019) were produced using modern lunar datasets to check and calibrate the lunar chronology function, because of the importance of these events to lunar/planetary chronologies. Similarly, the geologic mapping of the CE-5 landing site provides the basis on which to calibrate lunar/planetary chronology functions in the much younger 1-2 Ga timeframe (van der Bogert and Hiesinger, 2020). Due to the variability of ages determined for the regional mare during other broader studies, we select crater spatial density reference areas for the mare unit near the landing site and measure these specifically for the calibration of the chronology with the laboratory-measured radiometric ages.

To ensure that these key scientific questions can be addressed in the laboratory, it is critical to have a framework for the interpretation of the materials collected by CE-5. Thus, we produced a geological map and stratigraphic column, to help understand the origins of the diversity of sampled materials, and to place these into the current understanding of lunar history and evolution. Both the geological column and map can help the sample analysts to select key scientific questions in relation to the CE-5 samples, enhancing the results of these analyses.

2. Geological mapping

The CE-5 landing site is located in Northern Oceanus Procellarum, northeast of Mons Rümker (Fig. 1). The Rümker Quandrangle was first mapped by Scott and Eggleton (1973) (1:1M scale); they distinguished Imbrium-aged (Im) and Eratosthenian-aged (Em) mare basalts, highlands (Ith), and impact crater materials. More detailed geological maps of the Rümker region, which divided the units stratigraphically and number them in order of their formation ages, were produced by Zhao et al. (2017) and Qian et al. (2018), focusing on the candidate CE-5 landing region (41-45°N, 49-69°W); geologic units were subdivided into mare (Im1, Im2/P10, Im3, Em1, Em2, Em3, and Em4), Rümker plateau (IR1, IR2, and IR3), dome (sd, ld, and ldm), and highland (Ith) materials. Now that the precise location of the landing site is known (Fig. 2AB), small-scale geological mapping can be conducted to provide valuable local context for the samples. Thus, we mapped a region between 42-44°N and 40-53°W (Fig. 5). Data and methods

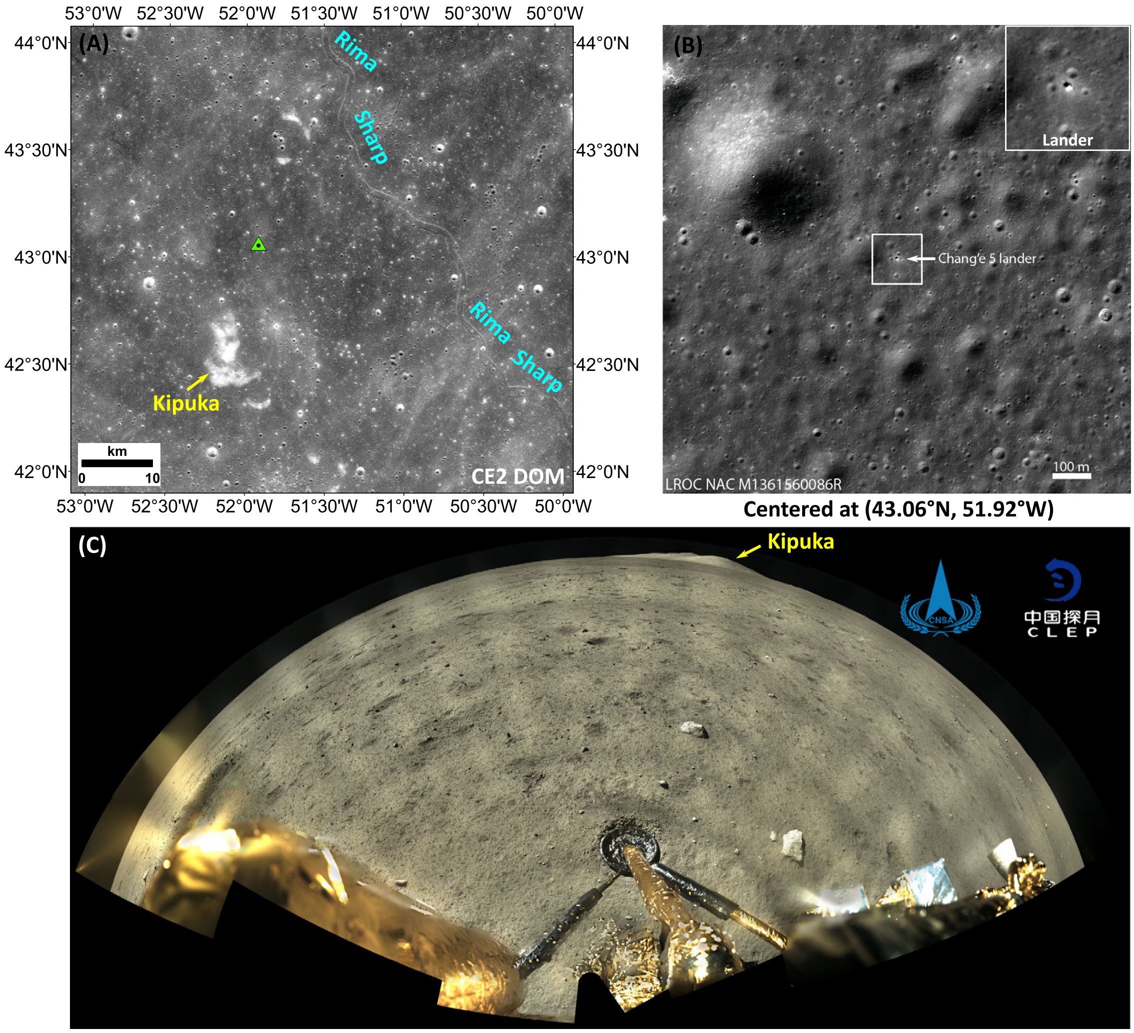

Fig. 2. (A, B) CE-5 landing site at 43.06°N, 51.92°W (green triangle) shown in the Chang'e-2 (CE-2) Digital Orthophoto Map (DOM) and LROC Narrow Angle Camera (NAC) datasets (white arrow), respectively. (C) Panoramic image of the landing site. The yellow arrow indicates the largest kipuka in the region. Rima Sharp is located to the east of the studying area, covered mainly by NE-SW ejecta.

used to derive the geological map are described in the Supplemental Material (Note S1).

Based on the methodology outlined, the CE-5 landing site was classified into three major geological units (mare basalt, highland, and impact crater materials); structures (sinuous rilles, wrinkle ridges) were also mapped.

2.1. Mare basalts

The dominant geologic unit in the landing region is a morphologically and spectrally defined mare basalt, named P58 in Hiesinger et al. (2011, 2003) with an absolute model age (AMA) of 1.33 Ga, and defined as Em4 in the geological map of Qian et al. (2018) with an AMA of 1.21 Ga; Em4 and P58 have slightly different borders. Our detailed geological investigation reveals that although there are minor compositional variations in the mapped mare, almost all of these variations are related to crater rays/clusters from distant, usually, non-mare sources, which tend to lower the mare Ti content by surficial mixing (Fig. 3BC; see also Section 4); therefore we find that no further subdivision of the mare unit is warranted at this scale. We designate the mare unit as "Em4/P58", representing the "Eratosthenian-aged mare basaltic unit". The AMAs of Em4/P58 are updated and assessed in Section 3 to provide landing site-specific results for comparison with radiometric sample ages.

Em4/P58 is a type of moderate-Ti mare basalt with an estimated TiO_2 abundance of 5-8 wt.% (Fig. 3B) and FeO abundance of 16.5-17.5 wt.% (Fig. 3C). Pyroxene (PYX) is interpreted to be the major mineral type, identified by strong absorptions at 1 and 2 μm (Qian et al., 2021); together, yielding a greenish hue in the Moon Mineralogy Mapper (M^3) Integrated-Band-Depth (IBD) color composite map (Fig. 3F). The absolute mineral abundances of clinopyroxene (CPX), orthopyroxene (OPX), olivine (OLV), and plagioclase (PLG) are estimated based on the Kaguya Multiband Imager (MI) data (Lemelin et al., 2019) (CPX, ∼31, OPX, ∼15, OLV, ∼13 and PLG ∼41 wt.%, assuming CPX + OPX + OLV + PLG = 100 wt.%, Fig. S1). If assuming all TiO_2 are stored in ilmenite (ILM) and CPX + OPX + OLV + PLG + ILM = 100 wt.%, it gives the abundances of CPX, OPX, OLV, PLG, and ILM are 27, 13, 11, 36, and 12 wt.%, respectively. The original TiO_2 content of fresh mare basalts may be higher, and PLG may be lower, because of widespread regolith contamination by crater rays of non-mare origin (Fig. 3BC).

The formation and emplacement mechanism of Em4/P58 mare basalts is not well-understood. Rima Sharp, the longest lunar sinuous rille (Hurwitz et al., 2013), extends across the unit and is thought to be one of the major sources of Em4/P58 (Qian et al., 2021). Underlying dikes may be another source, but no evidence of eruptive fissures or flow fronts are seen within the unit.

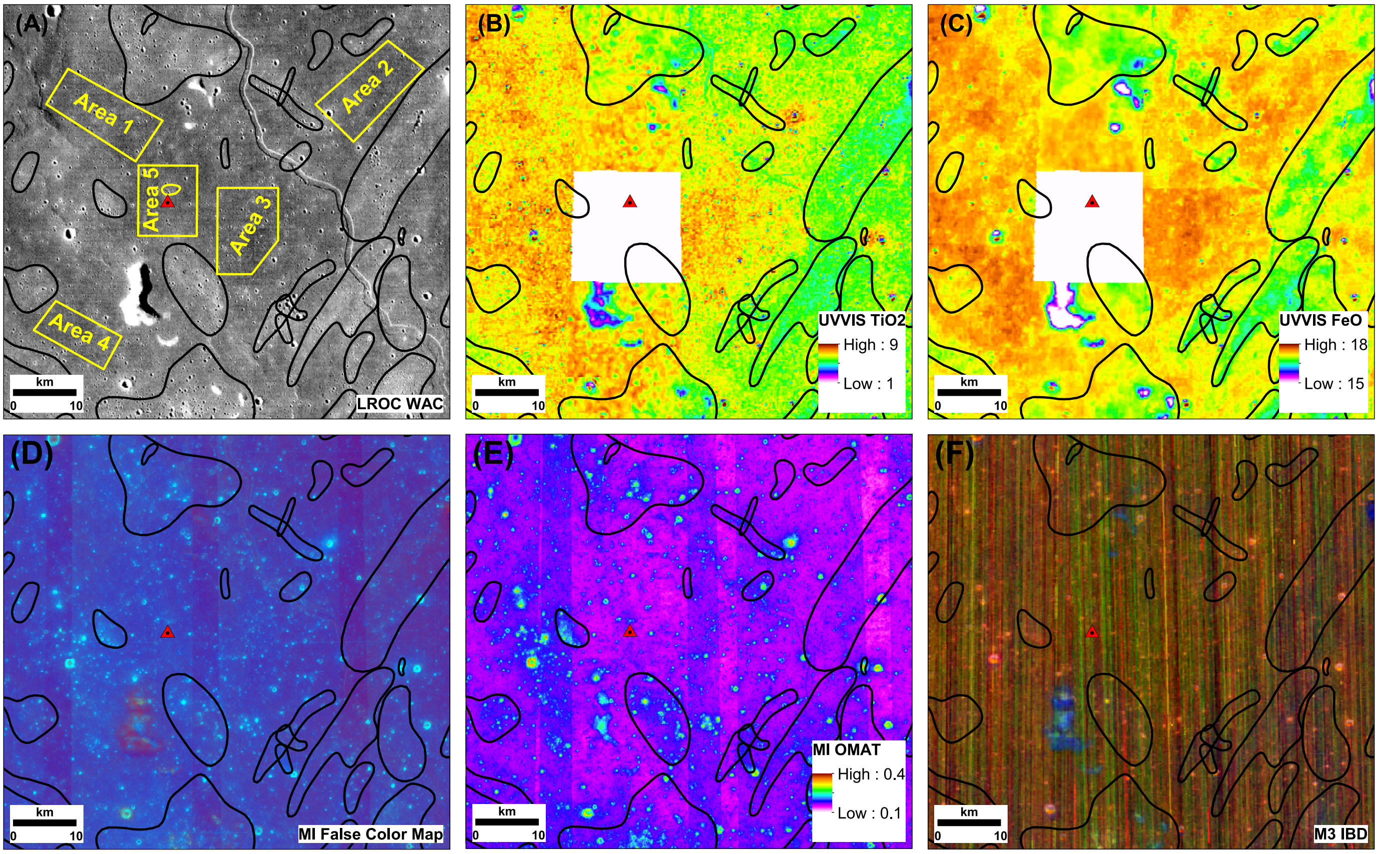

Fig. 3. (A) LROC Wide Angle Camera image, (B) Clementine TiO_2 abundance, (C) Clementine FeO abundance, (D) MI false-color map, and (E) M^3 IBD color composite map of the mapped area. The red triangle represents the CE-5 landing site, the black lines represent distal ejecta (see also Section 4), and the crater counting areas are outlined by yellow lines. The distal ejecta have a preferred direction of NE-SW.

2.2. Highlands

The highlands are the non-mare materials within the mapped area (unit Ith of Scott and Eggleton, 1973) and described as hilly to hummocky small patches resembling the Alpes Formation. We concur with their description and classification and map the hilly, small patches within the region as Imbrian hilly terra (Ith).

There are seven Ith occurrences within the study area. They have a higher albedo and their surfaces are smoother and more degraded than the mare surface (Fig. 4H), due to more prominent downslope movement on steep slopes and relatively older ages. Ith outcrops are kipukas, embayed by Em4/P58. Raised crater rims classified as Ith are remnants of mostly flooded craters (Fig. 4H). Ith was interpreted previously as ejecta of the Iridum impact (Scott and Eggleton, 1973), occurring at ~3.9 Ga (Ivanov et al., 2016).

Ith has very low TiO_2 and FeO abundances, due to the very low abundances of mafic minerals (Fig. 3BC) in highland materials. The PLG abundance of Ith is much higher than for the mare, as shown by the blue color in M^3 IBD color-composite map (Fig. 3F), with an abundance of ~50-60 wt.% (Fig. S1F).

2.3. Impact craters

Impact crater-related features are subdivided into six categories: Copernican craters, Eratosthenian craters, crater chains, crater clusters, ghost craters, and buried craters. No Imbrian-aged craters have been identified in the mapped region, consistent with the Eratosthenian-aged mare surface (Qian et al., 2021, 2018). Some ghost craters are likely Imbrian-aged although others may be early Eratosthenian; we classified them according to their unusual morphology, i.e., ghost craters.

Copernican crater units (Cc, Ccm, Ccr): Copernican craters (Cc) have sharp rims, prominent ejecta (Ccm) and rays (Ccr) (Fig. 4AB). Copernican craters have high optical maturity values (OMAT) and albedos. The presence of distinctive ejecta and/or rays is the primary diagnostic characteristic for a Copernican age (Fig. 4A), which is identified also in the OMAT maps (Fig. 4B). Some crater chains and clusters are Copernican in age, classified separately, and mapped as crater chains or crater clusters.

Eratosthenian crater units (Ec, Ecm): Eratosthenian craters (Ec) have sharp rims and degraded ejecta (Ecm), and do not have high albedo or immaturity rays. Their OMAT values and albedos are much lower than those of Copernican-aged craters, especially without abundant ejecta and no rays at all (Fig. 4DE). Some crater chains and clusters are Eratosthenian-aged, but we map them as separate units.

Crater chain unit: Crater chains typically form a line of similar-sized secondary impact craters (Fig. 4C). They have a high albedo (both from immaturity and contamination of the bright highland material). They usually have shallow depths, and often overlap each other, with some crater chains developing herringbone patterns, with the “V” pointing back to the parent crater. Crater chains are products of satellite craters oriented radially around their primary craters. In the mapped area, most crater chains can be traced back to parent craters Aristarchus, Copernicus, Harpalus, Kepler, and Rümker E, determined according to the orientation of their long axes and/or herringbone patterns (see also Section 4).

Crater cluster unit: In contrast to crater chains, crater clusters are less-linear groupings of similar-sized craters that often overlap one another (Fig. 4F). Some are very degraded with reduced crater rim heights. Crater clusters are produced by collections of

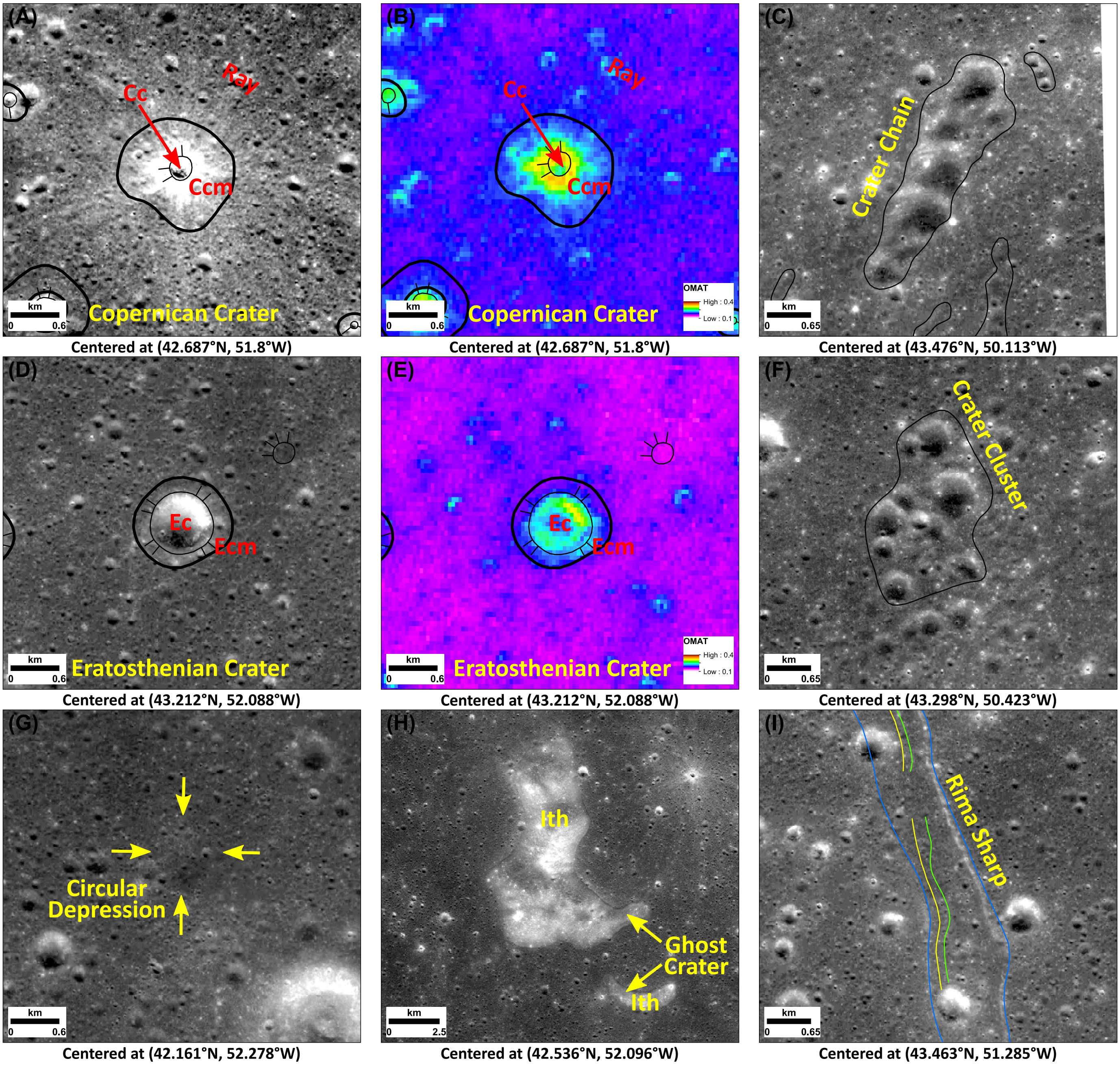

Fig. 4. Morphological features of the CE-5 region. (A, B) Copernican craters, (C) Crater chains, (D, E) Eratosthenian craters, (F) Crater clusters, (G) Circular depression, indicating an entirely buried crater, (H) Highlands exposures and ghost craters, and (H) Rima Sharp, which exhibits inner rilles (yellow) and inner levees (green). The basemaps are CE-2 DOM images.

secondary craters, but their source craters cannot readily be traced, due to the absence of obvious directional orientations.

Ghost crater unit: Ghost craters are partially buried craters, usually occurring in proximity to exposed highlands (Fig. 4H). The majority of ghost craters are buried by Em4/P58, with portions of their less mafic rims protruding above the embaying flat mare unit. Based on their size and orientation, these craters may be satellite craters of the Iridum impact (Scott and Eggleton, 1973), widely distributed in highlands east of Em4/P58.

Buried crater unit: Buried craters are entirely buried circular landforms (Fig. 4G). They are identified based on the presence of a circular depression in the mare surface. They can be distinguished from strongly degraded craters by the absence of protruding rim segments, and their size (∼1 km). In the mapped area of the Eratosthenian-aged mare surface, we found no primary craters in the size range of the ∼1 km circular depressions that had been degraded to this extent; thus, this adds support to the interpretation that they are pre-mare impact craters that have been flooded during emplacement of Em4/P58.

2.4. Structures

Wrinkle ridges: Wrinkle ridges are linear to sinuous tectonic features (Watters, 1988) primarily distributed in the western mapped area (Fig. 3A). They usually have a gently sloping broad arch at their base and a sharp irregular ridge at the summit. Wrinkle ridges in the area are predominantly orientated NW-SE, reflecting the subsurface structures (Qian et al., 2018). Wrinkle ridge formation in the area appears to have been a continuous

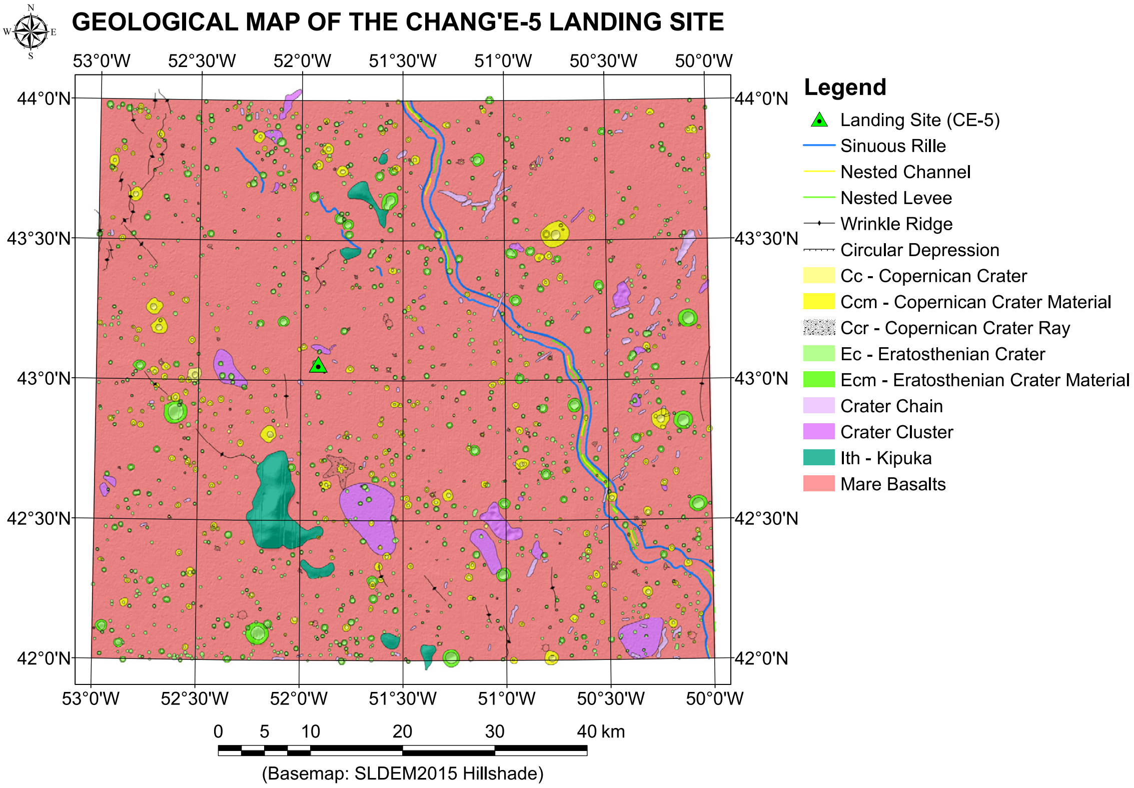

Fig. 5. Geological map of the CE-5 landing site (green triangle, 43.06°N, 51.92°W) in Northern Oceanus Procellarum. The definitions of different geological features and units are described in Section 2.

process, starting from as early as the Imbrian Period, and extending even to the current time (Watters et al., 2012; Yue et al., 2017).

Sinuous rilles: Sinuous rilles are volcanic channels that are concentrated in the eastern mapped area (Rima Sharp, Fig. 4I). Rima Sharp has been described as the longest lunar sinuous rille (Hurwitz et al., 2013), ~566 km long, 0.8-3 km wide, and 20-50 m deep (Qian et al., 2018). Rima Sharp traverses through the area from north to south, exhibiting a width of ~850 m and a depth of ~30 m. Nested features are observed within Rima Sharp, i.e., nested channels and nested levees (yellow and green lines, Fig. 4I), which may be the products of continuous and waning lava flow through Rima Sharp, or that entered Rima Sharp from a source in the south (Qian et al., 2021). Another small sinuous rille with a width of ~180 m lies completely within the northwest part of the area (Fig. 5).

3. Crater size-frequency distribution (CSFD) measurements on the mare basalts

The cumulative number of craters ≥a reference diameter, usually 1 km or N(1), coupled with the radiometric and exposure ages of lunar samples are critical for the calibration of the lunar chronology function (Hiesinger et al., 2012; Iqbal et al., 2020, 2019; Neukum et al., 2001; van der Bogert and Hiesinger, 2020). This calibration allows the dating of unsampled surfaces across the Moon and throughout the Solar System via CSFD measurements, which shed light on the history and evolution of the planets (Hiesinger et al., 2011). Given that there is no calibration point for the 1-3 Ga age range, a wide diversity of model ages for surface units are predicted by different chronology functions (Hiesinger et al., 2020; van der Bogert and Hiesinger, 2020). Thus, one of CE-5's most important objectives is to compare the N(1) values at the landing site with the radiometric ages of the CE-5 samples. Here, we report both AMAs, to provide easy comparison with prior results, and N(1) values using different production and chronology functions, that can be used for a new chronology calibration point (Table S2). Data and methods used to derive the AMAs are described in the Supplemental Material (Note S2).

Five areas were selected for measurement of CSFDs on Em4/P58 based on the homogeneity of albedo, morphology, TiO_2 and FeO abundance, and OMAT value maps (Fig. 3). Areas with low TiO_2 and FeO abundances or high OMAT values were excluded from the CSFD measurements because these areas are more likely to have been affected by extensive secondary craters/ejecta, consistent with our geological mapping (Fig. 5).

The results of the CSFD measurements are shown in Fig. 6. Areas 1-5 have ages, fitted using Poisson timing analysis and the Neukum et al. (2001) production and chronology functions, of $1.68^{+0.31}_{-0.32}$ Ga, $1.43^{+0.21}_{-0.21}$ Ga, $1.71^{+0.24}_{-0.24}$ Ga, $1.57^{+0.21}_{-0.21}$ Ga, and $1.60^{+0.16}_{-0.16}$ Ga, respectively. The N(1) values for each of these count areas, plus AMAs derived via cumulative fitting using both the Neukum (1983) and Neukum et al. (2001) production functions are presented in Table S2. CE-5 landed within Area 5, which exhibits an AMA of 1.6 Ga. These five ages are within error of each other, suggesting that the surface age of the CE-5 landing site is ~1.6-1.7 Ga. We detected no significant age variations within the mapped area.

4. Regolith materials: in-situ and exotic provenance

The entire mapped area is covered by a regolith layer originating from continuous impact bombardment following lava flow emplacement (McKay et al., 1991). The regolith consists of two components: 1) an in-situ component produced by impact reworking of the underlying mare basalt protolith (Head and Wilson, 2020, their Fig. 3) by micrometeorite rock breakup and comminution, and agglutination (quenched impact glass and glass-welded particles); 2) an exotic component, contributed to the regolith by ejecta from distant impact events and delivered to the site as crater rays

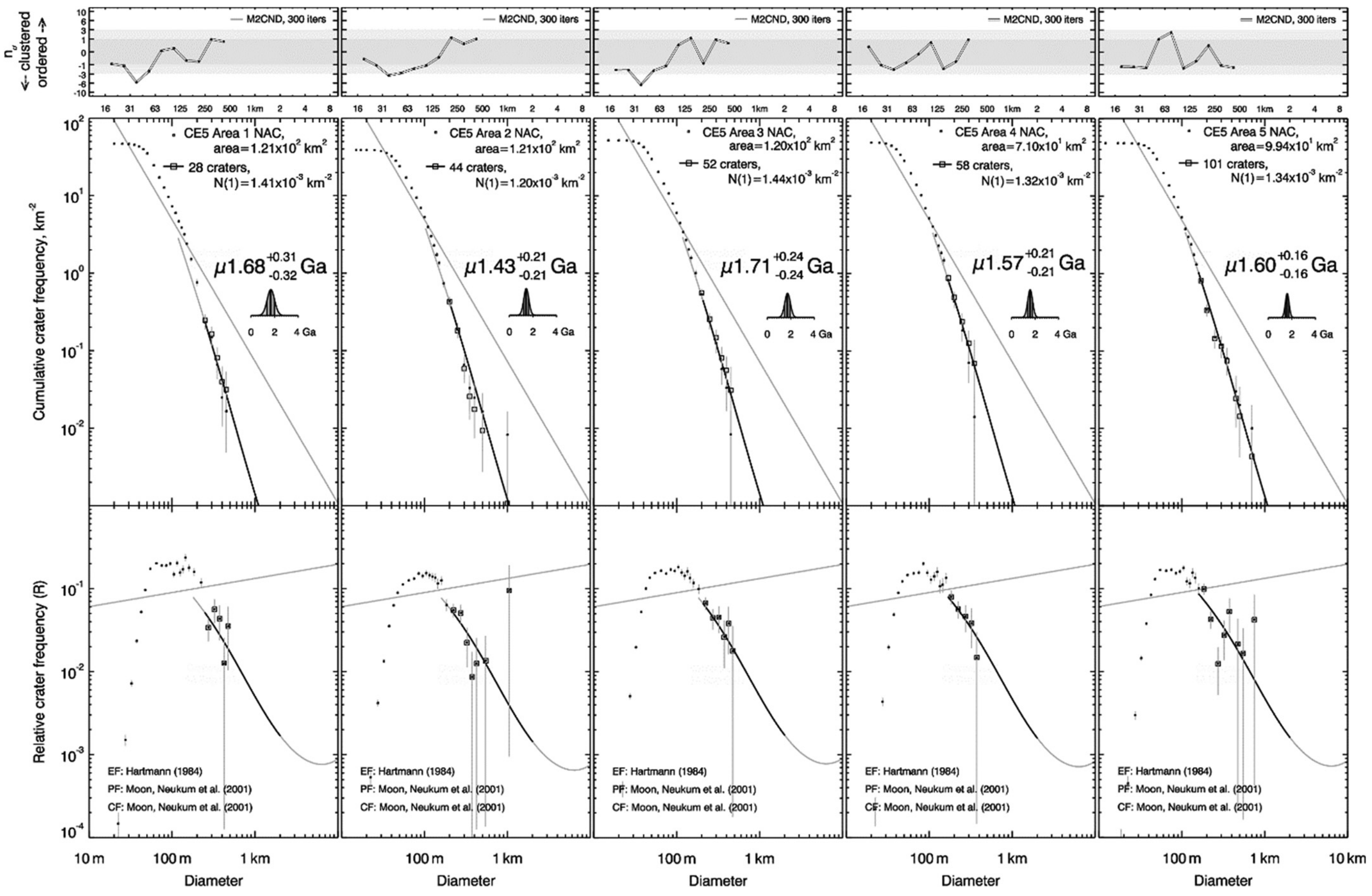

Fig. 6. Absolute model ages and $N(1)$ values derived from CSFD measurements for Areas 1-5 shown in Fig. 3A (see also Table S2). The CE-5 landing site is in area 5. The $N(1)$ values can be used in conjunction with laboratory radiometric age dates of the basalt samples to produce a new calibration point for the lunar cratering chronology.

and secondary craters; this component is volumetrically minor but regionally informative (Liu et al., 2021; see also Section 4.2).

Analysis of Apollo/Luna mare regolith showed two developmental stages of the in-situ regolith component (Head and Wilson, 2020): 1) initial buffering trend: early coarse-grained/blocky protolith substrate ejecta undergoes continuous impact bombardment reducing grain size, and adding agglutinates to the soil, reworking already-existing regolith. Eventually, this thickening regolith layer acts as a buffer to additional regolith growth, favoring reworking over further breakup of the mare basalt protolith. 2) impact flux trend: Eventually, decreasing impact flux lowers the bombardment rate of older flows (thus the regolith growth rate will be nonlinear). This means that younger lava flows (such as Em4/P58) are subject to both a lower integrated impact flux and a lower absolute flux. We thus predict that the CE-5 regolith component will be coarser-grained, blockier, and much thinner than that at the Apollo-11/12/15/17 mare landing sites, all at least twice as old as CE-5.

The exotic components contributed to the site from distant craters are very important as they provide unique samples of a much wider area of the lunar crust (e.g., the Copernicus ejecta and non-mare breccias in the Apollo 12 landing site; Barra et al., 2006; Jolliff et al., 2000b). Thus, estimating the sources of these components is of critical interest to sample analysts, and we describe these in the following section.

The sources of exotic materials at the CE-5 landing site were initially studied by Qian et al. (2018) and Xie et al. (2020). Xie et al. (2020) selected ten candidate ejecta source craters (Aristarchus, Pythagoras, Hausen, Robertson, Aristoteles, Langrenus, Harpalus, Philolaus, Copernicus, Sharp B, and Carpenter), and then applied CSFD measurements to the continuous ejecta of each crater to determine which may be post-mare in age (only source craters younger than Em4/P58 can be candidate sources). They then used ballistic sedimentation models to calculate the ejecta thickness at the CE-5 site for each crater. Xie et al. (2020) proposed that ~12-13% of exotic materials should be found in Em4/P58 regolith, mainly from Aristarchus, Copernicus, Sharp B, and Harding. Thus, the in-situ component dominates the regolith in the CE-5 landing region. We note, however, that CE-5 actually landed outside their study area, which was smaller than the nominal CE-5 landing region. In addition, the detailed ejecta mapping undertaken in our study (Section 4.1) shows that the ejecta in Em4/P58 have a dominant direction of NW-SW, suggesting Aristarchus and Copernicus are not major ejecta source craters for Em4/P58, contrasting with Xie et al. (2020)'s results. To resolve these discrepancies, we examine source crater ejecta distributions and their thicknesses within our study area.

4.1. Ejecta distribution from distant impacts

In contrast to the 1.6-1.7 Ga age range we determined immediately surrounding the CE-5 landing site, the overall Em4/P58 unit has a late-Eratosthenian age (~1.53 Ga, with some variations; Qian et al., 2021); all pre-Eratosthenian craters and most Eratosthenian craters nearby are not ejecta source craters. Calling on the initial global selection of Xie et al. (2020), their ejecta thickness calculation, and our regional investigation of young craters, we propose that Aristarchus, Copernicus, Harding, Harpalus, Kepler, Lichtenberg, Pythagoras, and Sharp B are the potential main source craters for foreign materials in this region (Fig. S2). Although Rümker E is relatively smaller than the others (6.76 km in diameter), it is close to Em4/P58 and its ejecta is easily distinguished from the mare

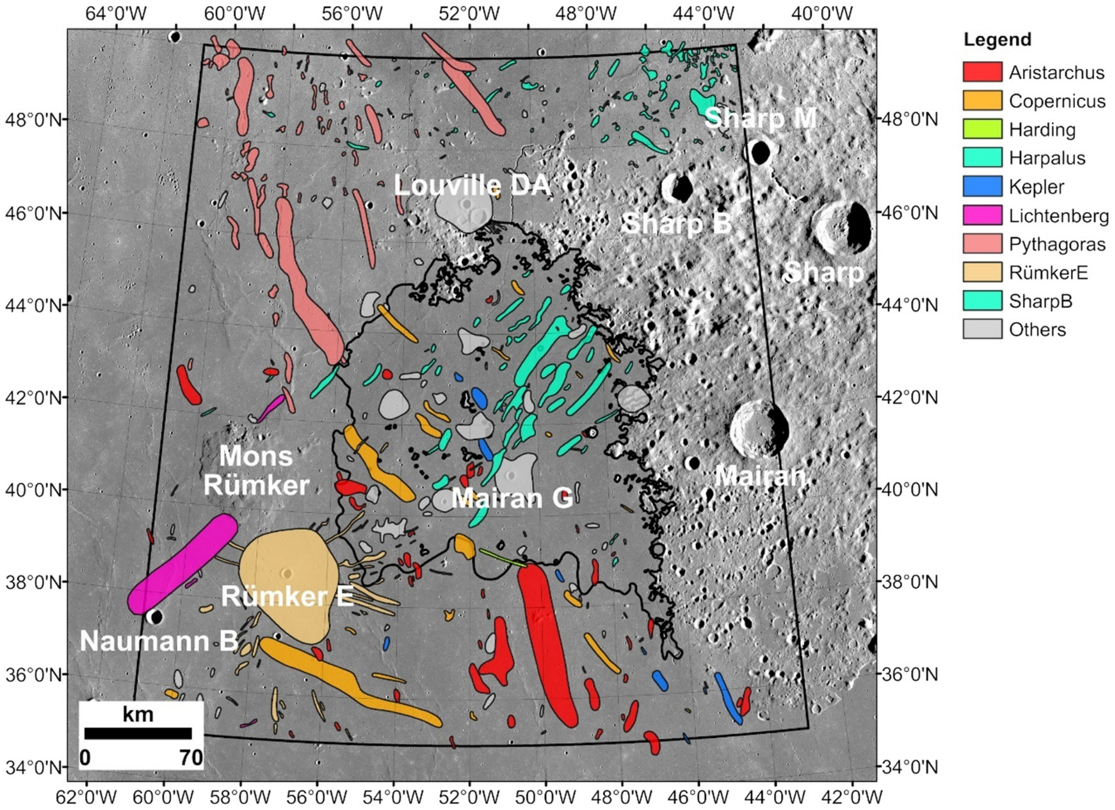

Fig. 7. Ejecta distribution of major source craters in the Northern Oceanus Procellarum. See the regional context in Fig. 1. The basemap is Kaguya Terrain Camera Morning Map.

Table 1
Main source craters and calculated ejecta thickness for Em4/P58.

	Diameter (km)	Longitude (°)	Latitude (°)	AMAs (Ga)	Total Ejecta Thickness (cm)[i]	Percentage in Regolith (%)[j]
Post-Em4/P58						
Rümker E	6.76	−57.14	38.64	/	0.1 (0.06)	0.08
Aristarchus	40.14	−47.49	23.74	280 Ma[a]	2.6 (0.8)	1.1
Kepler	30.12	−38.00	8.11	625-950 Ma[b]	0.2 (0.04)	0.05
Copernicus	94.30	−20.06	9.64	779 Ma[c] 796 Ma[d] 782 Ma[e]	7.6 (1.3)	1.8
Harding	23.04	−71.68	43.54	881 Ma[f]	0.8 (0.3)	0.4
Harpalus	39.77	−43.49	52.73	2.40 Ga[f,k] 3.50 Ga[g,k]	10.3 (4.2)	5.7
In total					21.6	9.1
Pre-Em4/P58						
Lichtenberg	19.53	−67.72	31.85	>1.68 Ga[h]	/	/
Sharp B	20.96	−45.34	47.00	1.15 Ga[f,k] 1.58 Ga[g,k]	5.6 (3.0)	/
Pythagoras	144.55	−62.98	63.68	2.68 Ga[f]	166.0 (46.4)	/

[a] Zanetti et al. (2017), [b] Koenig et al. (1977), [c] Hiesinger et al. (2012), [d] Iqbal et al. (2020), [e] Barra et al. (2006), [f] Xie et al. (2020), [g] THIS STUDY, [h] Hawke et al. (2004). [i] The total ejecta thickness equals the thickness of source crater ejecta (numbers in the brackets) and local materials excavated by the coming impact ejecta. [j] Contributions from each source craters to the top ~74 cm of lunar regolith (see Section 4.2). [k] We propose that directly counting Harpalus and Sharp B crater will produce unreliable AMAs (see Section 4.1).

basalts located southeast of Mons Rümker (Fig. 7). Thus, Rümker E's contribution is also considered.

To determine post-Em4/P58 craters, we first conducted a comprehensive literature study of these nine craters to collect their AMAs or relative ages (Table 1). Aristarchus (280 Ma, Zanetti et al., 2017), Copernicus (779-782 Ma, Barra et al., 2006; Hiesinger et al., 2012; Iqbal et al., 2020), Harding (881 Ma, Xie et al., 2020), and Kepler (625-950 Ma, Koenig et al., 1977) are Copernican-aged and dramatically younger than ~1.53 Ga, and their ejecta inevitably overlies the Em4/P58. Lichtenberg (>1.68 Ga, Hawke et al., 2004) and Pythagoras (2.68 Ga, Xie et al., 2020) are older than 1.53 Ga, therefore, they are unlikely to be ejecta source craters for Em4/P58.

To the east of Em4/P58, albedo and compositional data show abundant ejecta with a NE-SW direction (Figs. 3 and 7); thus, we infer that the NE-SW orientated ejecta should dominate the ejecta composition because of their extensive areal distribution. Ejecta tracing back to the parent craters (Fig. S3) indicate an origin either from Harpalus or Sharp B or both. According to the Xie et al. (2020) CSFD measurements, Harpalus has an AMA of ∼2.40 Ga, and Sharp B has an AMA of ∼ 1.15 Ga, suggesting that NE-SW ejecta are from Sharp B rather than Harpalus. However, more detailed morphological and compositional investigations of Harpalus and Sharp B craters show that Harpalus has a much younger appearance, with distinct high albedo radial ejecta with low-Ti and low-Fe materials excavated by this impact (Fig. S4). Sharp B crater has a more subdued morphology, without clear radial ejecta and excavated compositional halos (Fig. S4). Based on their morphology and degradation state, Harpalus is likely to be Copernican-aged and Sharp B should be Eratosthian-aged or even older. We also determined AMAs for Harpalus (3.5 Ga) and Sharp B (1.6 Ga) craters (Fig. S5), and determined Harpalus is older than Sharp B, the same age relationship determined by Xie et al. (2020). However, CSFD measurements on continuous ejecta of impact craters may be subject to contamination by secondary craters, self-secondary craters, and partially buried craters, which may give artificially older ages (Xiao, 2018; Zanetti et al., 2017). In contrast, because of higher slopes, the crater rim enhanced surface degradation rate may decrease the CSFD ages. Due to these unknowns, we chose to rely on the morphologically-defined age classification of Harpalus as a Copernican crater and Sharp B crater as an older, perhaps Eratosthenian-aged or even older crater. Their relative ages are also supported by 1) the global Copernican crater catalog (Ravi et al., 2016) based on OMATs (Harpalus is Copernican in the catalog but Sharp B is not); 2) Harpalus overlies Eratosthenian-aged P50 mare basalts (Hiesinger et al., 2011). We conclude that the NE-SW orientated ejecta, which is the dominant ejecta pattern in Em4/P58 and mapped area, originated from Harpalus crater (Fig. 7).

After we examined the main source craters of ejecta in the mapped region, we conducted a thorough investigation of ejecta in Em4/P58 using their long axis directions (Fig. S3); the ejecta was traced back to one of the nine listed craters. If its direction does not belong to any of these, it is labeled as “Others”. According to the resulting ejecta map (Fig. 7), the eastern part of Em4/P58 is covered by extensive ejecta from Harpalus crater, which can be traced continuously back to its source. “Other” ejecta have the second-largest coverage, either from local impacts (e.g., Mairan G) or distal impacts whose ejecta does not produce clear major orientations. Three large Copernican craters to the southeast of Em4/P58 (Aristarchus, Copernicus, and Kepler) also provide a significant amount of ejecta, especially Copernicus crater. The ejecta from Pythagoras is mainly distributed in the northwest study region, and contributes to the exotic ejecta composition of the older Imbrian-aged mare basalts, confirming the results of Xie et al. (2020). Pythagoras ejecta does not appear to overlie Em4/P58. Although ejecta from Rümker E are distinct to the southeast of Mons Rümker, they are localized because of the small diameter of Rümker E and should not have contributed to the exotic regolith component at the landing site.

4.2. *Exotic component ejecta thickness & percentage*

To quantitatively analyze the contribution from different distant ejecta sources, we calculated their thicknesses in the study region using the power-law model modified by Huang et al. (2018) that was applied to the CE-4 site, and showed good agreement with Lunar Penetrating Radar results (Lai et al., 2020). The model assumes the relation between r (the distance to the crater center), R (final crater radius), and T (ejecta thickness) is: $T = 3.95R^{0.399}(r/R)^{-3}$. The excavation efficiency (μ) of crater ejecta is: $\mu = 2.25 \times 10^{-5} r^{0.87}$, and the total ejecta thickness equals the sum of ejecta from other craters and excavated local material.

According to this calculation (Fig. 8, Table 1) of the exotic contributions, Harpalus contributes the most ejecta to Em4/P58 (∼10 cm), followed by two Copernican-aged craters Copernicus (∼8 cm) and Aristarchus (∼3 cm). Contributions from Kepler and Rümker E are nearly negligible. The ejecta thickness calculation agrees well with the ejecta distribution tracing (Fig. 7), suggesting Harpalus is the main ejecta source, dominating the overall ejecta thickness for Em4/P58 (Fig. S6). Pythagoras crater, with a diameter of ∼145 km, provides a significant amount of ejecta to Northern Oceanus Procellarum (∼166 cm), but it predates Em4/P58; its ejecta extensively overlies the Imbrian-aged mare basalts NW of the study region (Im2/P10), even extending to the Imbrian-aged mare basalt buried by Em4/P58. Sharp B crater is older than Em4/P58 based on its morphological characteristics (Section 4.1), thus its ejecta does not overlie Em4/P58, but could lie between Em4/P58 and Im2/P10, forming exotic paleo-ejecta contributions.

The percentage of contributions from each ejecta source crater to the landing site was calculated to first-order by employing Costello et al. (2018)’s regolith gardening model. The overturn depth function for at 99% probability is: $\Lambda = 3.45 \times 10^{-5} t^{0.47}$ (at least one overturn, Λ is the reworking depth in meters, t is reworking time in years; Costello et al., 2020). Considering the CE-5 mare basalts have an age of ∼1.65 Ga (between 1.6-1.7 Ga), the top ∼74 cm regolith is mixed up. Because the total ejecta thickness from studied source craters is ∼22 cm, we can assume all ejecta layers are mixed into the first ∼74 cm of lunar regolith. This yields the overall exotic components at the CE-5 landing site of ∼9% (Table 1), agreeing with the result of Xie et al. (2020) (10%). Harpalus (∼6%), Copernicus (∼2%), and Aristarchus (∼1%) are the three most important source craters.

5. Discussion

5.1. *Chronology of the CE-5 landing site*

Em4/P58 has been dated by different workers using CSFD methods (discussed in detail by Qian et al., 2021). In summary, Hiesinger et al. (2011, 2003), Wu et al. (2018), and Qian et al. (2021, 2018) determined a young age for Em4/P58; all their derived ages are younger than 1.6 Ga (Table S1). Morota et al. (2011) and Jia et al. (2020) proposed an intermediate age for Em4/P58 (∼2.0 Ga). However, their count areas appear to include many secondary craters, which can make the age determinations older (see also Fig. 6 in Qian et al., 2021). Giguere et al. (2020) obtained an older age (3.05 Ga) within the P58 count area of Hiesinger et al. (2003) and an age of 3.33 Ga in the vicinity of the Mairan dome outside of the original P58 count area. The older ages obtained by Giguere et al. (2020) likely represent the age of underlying early Eratosthenian and later mare basalts (Qian et al., 2021), which have been buried to differing extents across the region. Particularly in the area around the Mairan domes, the younger flows are likely not as thick or may not have completely flooded around the domes due to the slightly higher elevations near the basin edge.

For this study, we carefully selected areas at and around the landing site, which can be interpreted to represent the geological unit from which the CE-5 samples were collected. Thus, we paid particular attention to the selection of areas with minimal secondary craters, chains, and clusters, and with minimal spectral variation to ensure a single homogeneous geological unit for the measurements. All five of the count areas give ages within the error of each other with a range from 1.6-1.7 Ga. These new ages are consistent with the young ages determined during the earlier studies discussed above. A complete listing of the AMAs and N(1) values determined using different fitting approaches and production functions can be found in Table S2. Of critical importance, however, the individual count area (Area 5) that contains the landing site gives an AMA of 1.6 Ga with an N(1) value of

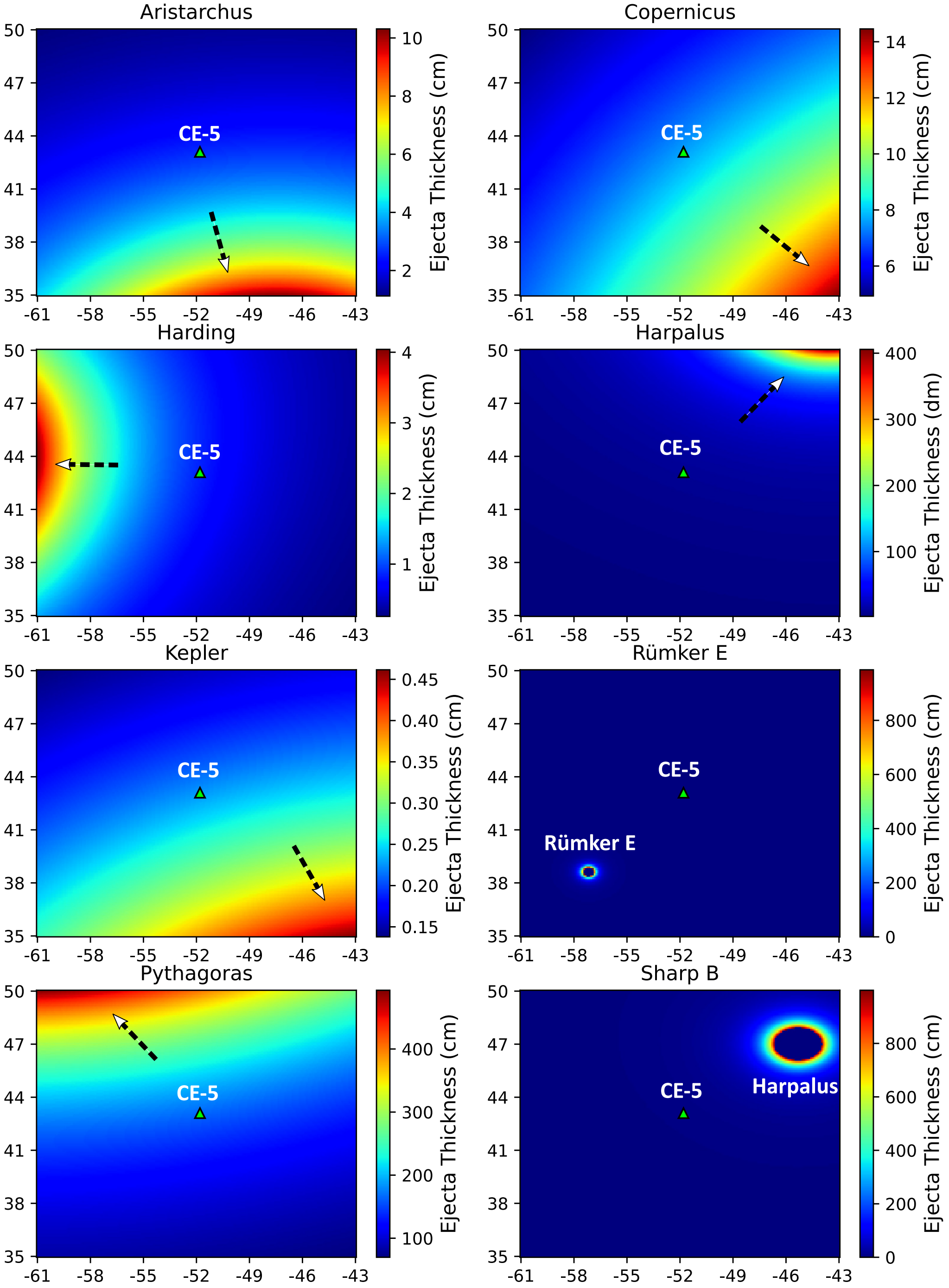

Fig. 8. Ejecta thickness of potential from the investigated craters. Pythagoras and Sharp B craters are older than Em4/P58. The x-axis and y-axis represent longitude and latitude, respectively. White arrows point to the ejecta source craters.

1.34×10^{-3} km^{-2} – a reference value that can be used to calibrate the lunar chronology in conjunction with radiometric ages of the CE-5 young samples.

The region mapped in the current study, which contains the landing site, lies within subunits 12-15 and 20-23 from (Qian et al., 2021) (Table S1, Fig. S7), where AMAs between 1.4-1.8 Ga were determined (Subunit 21 is excluded because of the high concentration of secondary craters). The AMAs of the five counting areas in the current study (1.6-1.7 Ga) are consistent with these results (1.4-1.8 Ga), which are also within the error of each other. This suggests that the surface age of the CE-5 landing region is nearly homogeneous, without significant variations.

However, these results do not mean that the CE-5 returned samples will only have ages around ~1.6-1.7 Ga, as local impacts may deliver younger or older mare basalts from the region to the site (Qian et al., 2021). Some of Em4/P58 contain large impacts that have penetrated through to underlying units such as the Imbrian-aged low-Ti mare basalts, forming low-Ti ejecta halos (Qian et al., 2021, 2018). This suggests that Imbrian-aged particles may also be present in the CE-5 samples. As discussed earlier, Harpalus, Copernicus, and Aristarchus craters are the three main source craters for remote ejecta contribution of exotic materials to the regolith. Nevertheless, the majority of the sampled material should be representative of the Em4/P58 basalts.

5.2. Additional exotic materials from adjacent and subjacent highlands, silicic domes, and meteoroids

As discussed in Section 4, Qian et al. (2018), and Xie et al. (2020), exotic materials are widely distributed in the CE-5 landing site and Northern Oceanus Procellarum. In addition to those delivered by distal impact (e.g., Harpalus, Copernicus, and Aristarchus), three other types of exotic materials have high scientific significance.

The first one is exotic components from subjacent and adjacent highlands by lateral mixing (Liu et al., 2021), for example, the Montes Jura (∼100 km distant), which was interpreted to be the Iridum ejecta deposits overlying Imbrium basin ejecta (Scott and Eggleton, 1973). According to remote sensing observations, the width of typical mare/highlands mixing zones is ∼4-5 km; however, even farther from the mare/highlands boundaries, there are >20% highland materials in some soil collections (Huang et al., 2017). Besides, the closest highlands (∼15 km in distance) to the CE-5 site are kipukas (Fig. 2A), labeled as "Ith" in our geological map (Fig. 5). These kipukas are interpreted as remnants of Iridum ejecta, partially buried by lateral eruptions of mare basalts (Qian et al., 2021, 2018). Any samples from highlands in the CE-5 collection, including rock fragments and impact melts, may provide significant information on the formation of the Iridum and Imbrium basins, and provide information on the subcrustal structures of PKT (Jolliff et al., 2000a).

The second type of exotic components may originate from silica-rich domes. Although there are no silica-rich domes within the mapping area (Fig. 5), two such domes are close to the CE-5 site (Fig. S8). The Mairan domes are located along the eastern boundary between Em4/P58 and highlands (Boyce et al., 2018), a distance of ∼80 km from the landing site. Gruithuisen domes are located to the south of Montes Jura (Ivanov et al., 2016), a distance of ∼320 km from the landing site. If CE-5 samples contain silicic fragments, they are most likely from the Mairan or Gruithuisen domes, delivered by impacts. The Apollo-12 non-mare materials are the best example of foreign silica components from lateral mixing (Barra et al., 2006). Any samples with silica-rich composition in the CE-5 collection will be meaningful for our understanding of this end number of lunar volcanism, which is not yet clearly understood (silicate liquid immiscibility or fractional crystallization or underplating? Head and Wilson, 2017; Wilson and Head, 2017).

In addition, meteoritic materials (<2%) may also exist in the CE-5 samples, as they were widely found in Apollo/Luna samples (McKay et al., 1991). The CE-5 landing site has ∼2% of Copernicus ejecta, and thus the meteoritic components from the parent meteoroid may also be preserved, potentially providing evidence of a sporadic meteoroid bombardment in the Earth-Moon system, approximately 800 Ma ago (Terada et al., 2020).

5.3. Stratigraphy of the CE-5 landing site

The stratigraphy of the landing site provides a solid basis for interpreting the sequence of events in this area and the context for the provenance of the samples collected from the lunar regolith. Thus, we constructed a geological column (Fig. 9) by combining the results from the different approaches outlined above and below.

The topmost layer is the lunar regolith, composed predominantly of a relatively immature in-situ component (Layer II) from the impact modification of the solidified young mare protolith (Em4/P58), mixed with exotic components (Layer I) from distant craters, primarily ejecta from Late Eratosthenian and Copernican craters (<∼1.53 Ga), especially Harpalus (∼6 wt.%), Copernicus (∼2 wt.%) and Aristarchus craters (∼1 wt.%, Section 4). Although the ray and secondary crater deposits in the regolith contain important exotic ejecta, the actual deposits are still dominated by local materials (∼91 wt.%). Furthermore, such secondary ejecta covers only parts of the Em4/P58 surface, because it is far from any continuous ejecta of the main source craters. The in-situ lunar regolith component developed on the moderate-Ti mare basalts bedrock over about ∼1.5 Ga of impact flux and space weathering (McKay et al., 1991). The regolith is predicted to have a thickness of ∼4-7 m at the CE-5 landing site, determined by the crater morphology method (Qian et al., 2020) based on LROC Narrow Angle Camera images. The CE-5 regolith layer has an elevated Th abundance (5-8.5 ppm), but whether this elevated Th component is inherent in the parent basalt regolith protolith or is an extraneous contribution to the regolith (brought in from ejecta from the surrounding PKT terrain) is a fundamental question that is still under debate (e.g., see Qian et al., 2021 and Zhang et al., 2021).

Layers III, IV, and V represent Eratosthenian-aged moderate-Ti mare basalts (Em4/P58 and Em3). Layer III mare basalts originated from the extensive eruptions of Rima Sharp (Fig. 5; see also Fig. 8 in Qian et al., 2021). The formation of a typical sinuous rille on the Moon requires hundreds of km^3 of lavas (Wilson and Head, 2017), and the lavas should have been deposited in the proximity of Rima Sharp, including the CE-5 landing site, only ∼15 km distance from Rima Sharp. Rima Sharp is the relic of the eruption channel. Layer IV may be produced by dike eruptions because this is the most common eruption style on the Moon (Head and Wilson, 2017); however, there is no direct evidence, and the existence of any dikes unrelated to the sinuous rille is an open question. Layer V (∼2.0 Ga) is at the bottom of the moderate-Ti mare basalts, buried by lateral eruptions of Em4/P58 (∼1.5 Ga), as evidenced by their relative ages and surface embayment relationships (Qian et al., 2018). However, on the west of Mons Rümker, Em3 mare basalts are not buried by Em4/P58. The internal boundaries between three moderate-Ti basalt layers cannot be determined, because their compositions are nearly identical (Qian et al., 2021, 2018). However, the total thickness of the moderate-Ti mare basalts, ∼50 m, was estimated using the crater excavation method (Qian et al., 2021), based on the compositional difference between the overlying moderate-Ti and underlying low-Ti mare basalts.

Underlying Layer V, Layer VI, and VII are paleo-ejecta and paleo-regolith layers, derived from the long exposure (∼2 Ga) to the space environment of Imbrian-aged low-Ti mare basalts (Layer VIII) after its emplacement, until being buried by the Eratosthenian-aged mare basalts. The composition of exotic paleo-ejecta is likely to be dominated by the Pythagoras impact (Section 4), like Im2 and other Imbrian-aged mare units in Northern Oceanus Procellarum (Xie et al., 2020). The thickness of the paleo-regolith layer is ∼10 m, calculated to a first-order by assuming a regolith growth of ∼5 mm/Myr (Hörz and Cintala, 1997). These paleo-regoliths develop on the low-Ti mare basalts (Layer VIII), and maybe the same as those occurring in western Northern Oceanus Procellaum (Im2; Qian et al., 2018). The thickness of Layer VIII is estimated to be around ∼900 m, considering the overall thickness of mare basalts in Northern Oceanus Procellarum (∼1000 m; Gong et al., 2016) from GRAIL gravity modeling and by subtracting the thickness of moderate-Ti mare basalts and ejecta/regolith layers.

Kaguya Lunar Sounder data found numerous layers beneath Oceanus Procellarum (Ono et al., 2009), which may represent the reflective surface between the Eratosthenian-aged (Layer III, IV, V) and Imbrian-aged mare basalts (Layer VIII) at least for Northern Oceanus Procellum. The existence of paleo-ejecta, paleo-regolith, and other subsurface structures are confirmed by the Lunar Penetrating Radar data onboard CE-3 and CE-4 missions (Lai et al., 2020; Xiao et al., 2015). Similarly, the Lunar Penetrating Radar onboard CE-5 (Li et al., 2019) can also be used to test the occurrence of underlying paleo-deposits and test and improve our geological column, which is critical to our understandings of the local geological history.

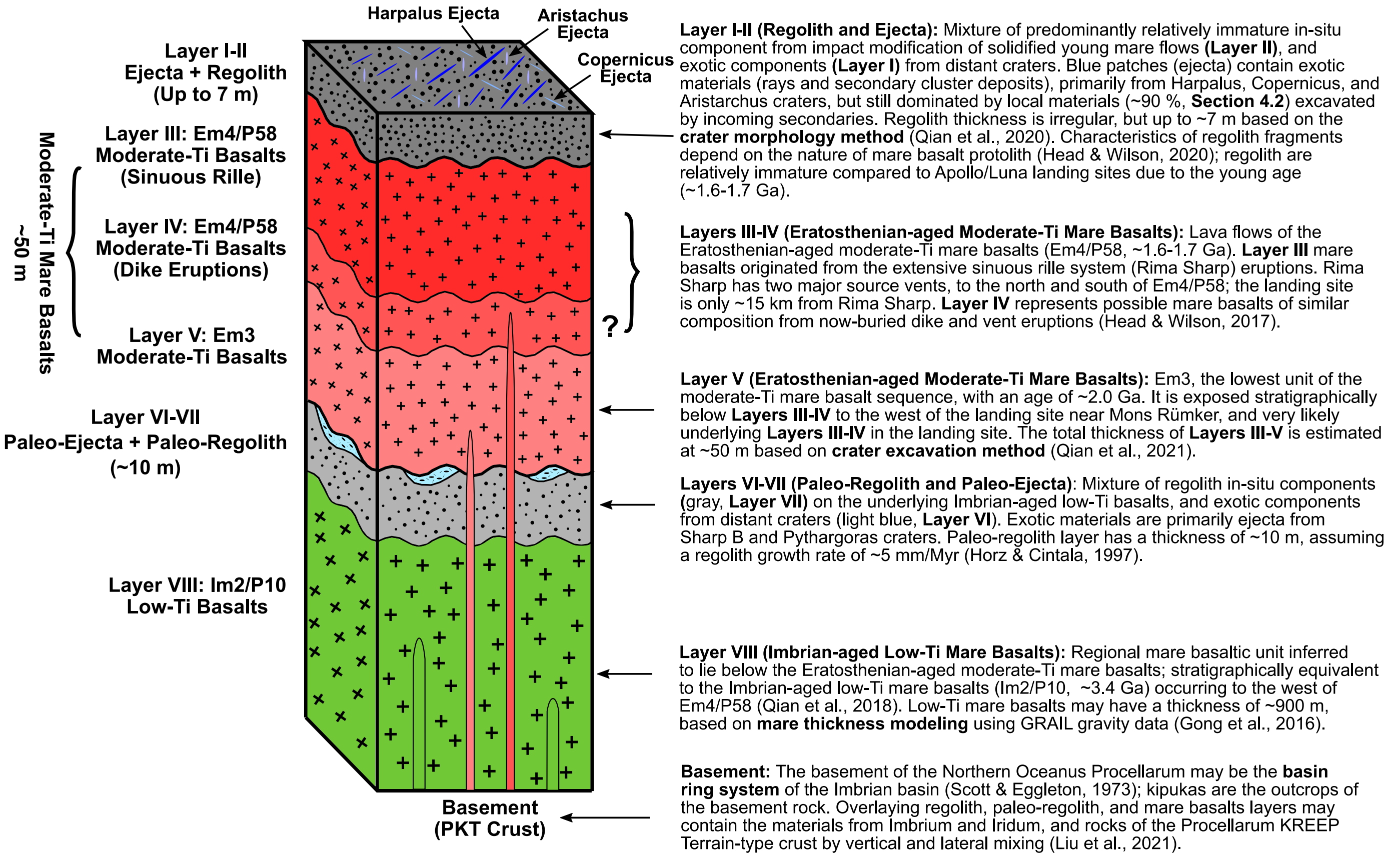

Layer I-II (Regolith and Ejecta): Mixture of predominantly relatively immature in-situ component from impact modification of solidified young mare flows **(Layer II)**, and exotic components **(Layer I)** from distant craters. Blue patches (ejecta) contain exotic materials (rays and secondary cluster deposits), primarily from Harpalus, Copernicus, and Aristarchus craters, but still dominated by local materials (~90 %, **Section 4.2**) excavated by incoming secondaries. Regolith thickness is irregular, but up to ~7 m based on the **crater morphology method** (Qian et al., 2020). Characteristics of regolith fragments depend on the nature of mare basalt protolith (Head & Wilson, 2020); regolith are relatively immature compared to Apollo/Luna landing sites due to the young age (~1.6-1.7 Ga).

Layers III-IV (Eratosthenian-aged Moderate-Ti Mare Basalts): Lava flows of the Eratosthenian-aged moderate-Ti mare basalts (Em4/P58, ~1.6-1.7 Ga). **Layer III** mare basalts originated from the extensive sinuous rille system (Rima Sharp) eruptions. Rima Sharp has two major source vents, to the north and south of Em4/P58; the landing site is only ~15 km from Rima Sharp. **Layer IV** represents possible mare basalts of similar composition from now-buried dike and vent eruptions (Head & Wilson, 2017).

Layer V (Eratosthenian-aged Moderate-Ti Mare Basalts): Em3, the lowest unit of the moderate-Ti mare basalt sequence, with an age of ~2.0 Ga. It is exposed stratigraphically below **Layers III-IV** to the west of the landing site near Mons Rümker, and very likely underlying **Layers III-IV** in the landing site. The total thickness of **Layers III-V** is estimated at ~50 m based on **crater excavation method** (Qian et al., 2021).

Layers VI-VII (Paleo-Regolith and Paleo-Ejecta): Mixture of regolith in-situ components (gray, **Layer VII)** on the underlying Imbrian-aged low-Ti basalts, and exotic components from distant craters (light blue, **Layer VI**). Exotic materials are primarily ejecta from Sharp B and Pythargoras craters. Paleo-regolith layer has a thickness of ~10 m, assuming a regolith growth rate of ~5 mm/Myr (Horz & Cintala, 1997).

Layer VIII (Imbrian-aged Low-Ti Mare Basalts): Regional mare basaltic unit inferred to lie below the Eratosthenian-aged moderate-Ti mare basalts; stratigraphically equivalent to the Imbrian-aged low-Ti mare basalts (Im2/P10, ~3.4 Ga) occurring to the west of Em4/P58 (Qian et al., 2018). Low-Ti mare basalts may have a thickness of ~900 m, based on **mare thickness modeling** using GRAIL gravity data (Gong et al., 2016).

Basement: The basement of the Northern Oceanus Procellarum may be the **basin ring system** of the Imbrian basin (Scott & Eggleton, 1973); kipukas are the outcrops of the basement rock. Overlaying regolith, paleo-regolith, and mare basalts layers may contain the materials from Imbrium and Iridum, and rocks of the Procellarum KREEP Terrain-type crust by vertical and lateral mixing (Liu et al., 2021).

Fig. 9. Geological column for the CE-5 landing site in Northern Oceanus Procellarum.

6. Conclusions

1) CE-5 landed at 43.06°N, 51.92°W in Northern Oceanus Procellarum, northwest of PKT, covered by Eratosthenian-aged (∼1.6-1.7 Ga) moderate-Ti mare basalts, with elevated Th abundance (inherent or extraneous); this is one of the youngest mare basalts on the Moon.

2) A geological map has been produced to serve as a basis for the provenance and interpretation of samples returned by CE-5 using the PLANMAP standard.

3) The geological map was used to define areas for measuring the N(1) values, for the landing site and four surrounding areas to serve as reference values for updating the lunar cratering chronology, in conjunction with radiometric ages from returned samples.

4) The Em4/P58 basalts were likely emplaced by Rima Sharp, the longest sinuous rille on the Moon, resulted from a major phase of a mare basalt eruption (Phase 2; Wilson and Head, 2018) with the later phases potentially exsolving volatiles to produce vesicular basalts.

5) The landing site is covered by a regolith layer (∼4-7 m), consisting of in-situ components developed on the young mare protolith and exotic components delivered by distant ejecta source craters. Exotic ejecta components are mainly from Harpalus (∼6 wt.%), followed by Copernicus (∼2 wt.%) and Aristarchus craters (∼1 wt.%), and may also contain high-Th content contributions from the surrounding PKT terrain. The ejecta from Harpalus has a NE-SW direction, and dominates the ejecta distribution in the eastern part of Em4/P58.

6) There are at least 9 different layers in the CE-5 landing site, including impact ejecta, regolith, moderate-Ti basalts, paleo-ejecta, paleo-regolith, low-Ti mare basalts, and PKT crust, which can be tested by Lunar Penetrating Radar onboard CE-5.

Declaration of competing interest

The authors declare that they have no known competing financial interests or personal relationships that could have appeared to influence the work reported in this paper.

Acknowledgements

The authors especially thank William McKinnon for his conscientious and helpful editorial assistance and two reviewers for their thoughtful suggestions which helped improve the paper. The authors wish to thank CNSA for organizing the Chang'e-5 mission. The authors thank Mark Robinson and the LROC team for imaging the CE-5 landing site immediately after the landing and kindly providing the international scientific community with the high-resolution LROC NAC image (http://lroc.sese.asu.edu/posts/1172). This research was funded by the National Key R&D Program of China (2020YFE0202100), the Pre-research Project on Civil Aerospace Technologies of CNSA (D020101, D020205), and the National Natural Science Foundation of China (41830214). YQ is funded by the China Scholarship Council 201906410015. JWH gratefully acknowledges funding for participation in the NASA Lunar Reconnaissance Orbiter Mission Lunar Orbiter Laser Altimeter (LOLA) Experiment Team (grant 80NSSC19K0605 from the National Aeronautics and Space Administration - Goddard). Carolyn van der Bogert and Harald Hiesinger are funded by the German Aerospace Center (Deutsches Zentrum für Luft- und Raumfahrt) project 50OW2001 and as part of a project that has received funding from the European Union's Horizon 2020 research and innovation programme under grant agreements N° 776276 (PLANMAP) and N° 871149 (Europlanet 2024 RI, GMAP). Xiaoming Lai, Guoxing Wang, Yong Pang, and Nai Zhang are funded by Civil Aerospace Technology Research Project (B0108).

Appendix A. Supplementary material

Supplementary material related to this article can be found online at https://doi.org/10.1016/j.epsl.2021.116855.

References

Barra, F., Swindle, T.D., Korotev, R.L., Jolliff, B.L., Zeigler, R.A., Olson, E., 2006. 40Ar/39Ar dating of Apollo 12 regolith: implications for the age of Copernicus and the source of nonmare materials. Geochim. Cosmochim. Acta 70, 6016–6031. https://doi.org/10.1016/j.gca.2006.09.013.

Boyce, J.M., Giguere, T., Mouginis-Mark, P., Glotch, T., Taylor, G.J., 2018. Geology of Mairan middle dome: its implication to silicic volcanism on the Moon. Planet. Space Sci. 162, 62–72. https://doi.org/10.1016/j.pss.2017.12.009.

Costello, E.S., Ghent, R.R., Hirabayashi, M., Lucey, P.G., 2020. Impact gardening as a constraint on the age, source, and evolution of ice on Mercury and the Moon. J. Geophys. Res., Planets 125, e2019JE006172. https://doi.org/10.1029/2019JE006172.

Costello, E.S., Ghent, R.R., Lucey, P.G., 2018. The mixing of lunar regolith: vital updates to a canonical model. Icarus 314, 327–344. https://doi.org/10.1016/j.icarus.2018.05.023.

Fagan, A.L., Neal, C.R., 2016. A new lunar high-Ti basalt type defined from clasts in Apollo 16 breccia 60639. Geochim. Cosmochim. Acta 173, 352–372. https://doi.org/10.1016/j.gca.2015.08.007.

Giguere, T.A., Boyce, J.M., Gillis-Davis, J.J., Stopar, J.D., 2020. Lava flows in northeastern Oceanus Procellarum: morphology, composition, and ages. In: 51st Lunar and Planetary Science Conference. Lunar and Planetary Institute, Houston. Abstract #2356.

Gong, S., Wieczorek Mark, A., Nimmo, F., Kiefer Walter, S., Head James, W., Huang, C., Smith David, E., Zuber Maria, T., 2016. Thicknesses of mare basalts on the Moon from gravity and topography. J. Geophys. Res., Planets 121, 854–870. https://doi.org/10.1002/2016JE005008.

Hawke, B.R., Blewett, D.T., Lucey, P.G., Smith, G.A., Bell, J.F., Campbell, B.A., Robinson, M.S., 2004. The origin of lunar crater rays. Icarus 170, 1–16. https://doi.org/10.1016/j.icarus.2004.02.013.

Head, J.W., Wilson, L., 2020. Rethinking lunar mare basalt regolith formation: new concepts of lava flow protolith and evolution of regolith thickness and internal structure. Geophys. Res. Lett. 47, e2020GL088334. https://doi.org/10.1029/2020GL088334.

Head, J.W., Wilson, L., 2017. Generation, ascent and eruption of magma on the Moon: new insights into source depths, magma supply, intrusions and effusive/explosive eruptions (Part 2: predicted emplacement processes and observations). Icarus 283, 176–223. https://doi.org/10.1016/j.icarus.2016.05.031.

Hiesinger, H., Bogert, C.H., Pasckert, J.H., Funcke, L., Giacomini, L., Ostrach, L.R., Robinson, M.S., 2012. How old are young lunar craters? J. Geophys. Res., Planets 117. https://doi.org/10.1029/2011JE003935.

Hiesinger, H., Head, J.W., Wolf, U., Jaumann, R., Neukum, G., 2011. Ages and stratigraphy of lunar mare basalts: a synthesis. Spec. Pap., Geol. Soc. Am. 477, 1–51. https://doi.org/10.1130/2011.2477(01).

Hiesinger, H., Head, J.W., Wolf, U., Jaumann, R., Neukum, G., 2003. Ages and stratigraphy of mare basalts in Oceanus Procellarum, Mare Nubium, Mare Cognitum, and Mare Insularum. J. Geophys. Res. E, Planets 108, 1. https://doi.org/10.1029/2002je001985.

Hiesinger, H., van der Bogert, C.H., Iqbal, W., Gebbing, T., 2020. The lunar chronology a status report. In: 51st Lunar Planet. Sci. Conf.

Hörz, F., Cintala, M., 1997. Impact experiments related to the evolution of planetary regoliths. Meteorit. Planet. Sci. 32, 179–209.

Huang, J., Xiao, Z., Flahaut, J., Martinot, M., Head, J., Xiao, X., Xie, M., Xiao, L., 2018. Geological characteristics of Von Kármán crater, northwestern South Pole-Aitken basin: Chang'E-4 landing site region. J. Geophys. Res., Planets 123, 1684–1700. https://doi.org/10.1029/2018JE005577.

Huang, Y.-H., Minton, D.A., Hirabayashi, M., Elliott, J.R., Richardson, J.E., Fassett, C.I., Zellner, N.E.B., 2017. Heterogeneous impact transport on the Moon. J. Geophys. Res., Planets 122, 1158–1180. https://doi.org/10.1002/2016JE005160.

Hurwitz, D.M., Head, J.W., Hiesinger, H., 2013. Lunar sinuous rilles: distribution, characteristics, and implications for their origin. Planet. Space Sci. 79–80, 1–38. https://doi.org/10.1016/j.pss.2012.10.019.

Iqbal, W., Hiesinger, H., van der Bogert, C.H., 2020. Geological mapping and chronology of lunar landing sites: Apollo 12. Icarus 352, 113991. https://doi.org/10.1016/j.icarus.2020.113991.

Iqbal, W., Hiesinger, H., van der Bogert, C.H., 2019. Geological mapping and chronology of lunar landing sites: Apollo 11. Icarus 333, 528–547. https://doi.org/10.1016/j.icarus.2019.06.020.

Ivanov, M.A., Head, J.W., Bystrov, A., 2016. The lunar Gruithuisen silicic extrusive domes: topographic configuration, morphology, ages, and internal structure. Icarus 273, 262–283. https://doi.org/10.1016/j.icarus.2015.12.015.

Jia, M., Yue, Z., Di, K., Liu, B., Liu, J., Michael, G., 2020. A catalogue of impact craters larger than 200 m and surface age analysis in the Chang'e-5 landing area. Earth Planet. Sci. Lett. 541, 116272. https://doi.org/10.1016/j.epsl.2020.116272.

Jolliff, B.L., Gillis, J.J., Haskin, L.A., Korotev, R.L., Wieczorek, M.A., 2000a. Major lunar crustal terranes: surface expressions and crust-mantle origins. J. Geophys. Res., Planets 105, 4197–4216. https://doi.org/10.1029/1999JE001103.

Jolliff, B.L., Gillis, J.J., Korotev, R.L., Haskin, L.A., 2000b. On the origin of nonmare materials at the Apollo 12 landing site. In: 31st Lunar Planet. Sci. Conf.

Koenig, B., Neukum, G., Fechtig, H., 1977. Recent lunar cratering: absolute ages of Kepler, Aristarchus, TYCHO. In: Eighth Lunar Sci. Conf.

Lai, J., Xu, Y., Bugiolacchi, R., Meng, X., Xiao, L., Xie, M., Liu, B., Di, K., Zhang, X., Zhou, B., Shen, S., Xu, L., 2020. First look by the Yutu-2 rover at the deep subsurface structure at the lunar farside. Nat. Commun. 11, 3426. https://doi.org/10.1038/s41467-020-17262-w.

Lemelin, M., Lucey, P.G., Miljković, K., Gaddis, L.R., Hare, T., Ohtake, M., 2019. The compositions of the lunar crust and upper mantle: spectral analysis of the inner rings of lunar impact basins. Planet. Space Sci. 165, 230–243. https://doi.org/10.1016/j.pss.2018.10.003.

Li, Y., Lu, W., Fang, G., Zhou, B., Shen, S., 2019. Performance verification of Lunar Regolith Penetrating Array Radar of Chang'E-5 mission. Adv. Space Res. 63, 2267–2278. https://doi.org/10.1016/j.asr.2018.12.012.

Liu, T., Michael, G., Zuschneid, W., Wünnemann, K., Oberst, J., 2021. Lunar megaregolith mixing by impacts: evaluation of the non-mare component of mare soils. Icarus 358, 114206. https://doi.org/10.1016/j.icarus.2020.114206.

McKay, D.S., Heiken, G., Basu, A., Blanford, G., Simon, S., Reedy, R., French, B.M., Papike, J., 1991. The lunar regolith. In: Heiken, G.H., Vaniman, D.T., French, B.M. (Eds.), Lunar Sourcebook: A User's Guide to the Moon. Cambridge University Press, pp. 285–356.

Morota, T., Haruyama, J., Ohtake, M., Matsunaga, T., Honda, C., Yokota, Y., Kimura, J., Ogawa, Y., Hirata, N., Demura, H., Iwasaki, A., Sugihara, T., Saiki, K., Nakamura, R., Kobayashi, S., Ishihara, Y., Takeda, H., Hiesinger, H., 2011. Timing and characteristics of the latest mare eruption on the Moon. Earth Planet. Sci. Lett. 302, 255–266. https://doi.org/10.1016/j.epsl.2010.12.028.

National Research Council, 2007. The Scientific Context for Exploration of the Moon. The National Academies Press, Washington, DC.

Neal, C.R., Hacker, M.D., Snyder, G.A., Taylor, L.A., Liu, Y.-G., Schmitt, R.A., 1994. Basalt generation at the Apollo 12 site, Part 1: new data, classification, and re-evaluation. Meteoritics 29, 334–348. https://doi.org/10.1111/j.1945-5100.1994.tb00597.x.

Neukum, G., 1983. Meteoritenbombardement und Datierung Planetarer Oberflaechen. University of Munich, Washington, DC.

Neukum, G., Ivanov, B.A., Hartmann, W.K., 2001. Cratering records in the inner solar system in relation to the lunar reference system. In: Kallenbach, R., Geiss, J., Hartmann, William K. (Eds.), Chronology and Evolution of Mars. Springer, Netherlands, Dordrecht, pp. 55–86.

Ono, T., Kumamoto, A., Nakagawa, H., Yamaguchi, Y., Oshigami, S., Yamaji, A., Kobayashi, T., Kasahara, Y., Oya, H., 2009. Lunar radar sounder observations of subsurface layers under the nearside maria of the Moon. Science 323, 909.

Pieters, C.M., Noble, S.K., 2016. Space weathering on airless bodies. J. Geophys. Res., Planets 121, 1865–1884. https://doi.org/10.1002/2016JE005128.

Qian, Y., Xiao, L., Head, J.W., van der Bogert, C.H., Hiesinger, H., Wilson, L., 2021. Young lunar mare basalts in the Chang'e-5 sample return region, northern Oceanus Procellarum. Earth Planet. Sci. Lett. 555, 116702. https://doi.org/10.1016/j.epsl.2020.116702.

Qian, Y., Xiao, L., Yin, S., Zhang, M., Zhao, S., Pang, Y., Wang, J., Wang, G., Head, J.W., 2020. The regolith properties of the Chang'e-5 landing region and the ground drilling experiments using lunar regolith simulants. Icarus 337, 113508. https://doi.org/10.1016/j.icarus.2019.113508.

Qian, Y., Xiao, L., Zhao, S., Zhao, J., Huang, J., Flahaut, J., Martinot, M., Head, J.W., Hiesinger, H., Wang, G., 2018. Geology and scientific significance of the Rümker region in northern Oceanus Procellarum: China's Chang'E-5 landing region. J. Geophys. Res., Planets 123, 1407–1430. https://doi.org/10.1029/2018JE005595.

Ravi, S., Mahanti, P., Meyer, H., Robinson, M.S., 2016. On the usefulness of optical maturity for relative age classification of fresh craters. In: American Geophysical Union Fall Meeting. San Francisco.

Scott, D.H., Eggleton, R.E., 1973. Geologic map of the Rumker Quadrangle of the Moon. IMAP. https://doi.org/10.3133/i805.

Tartèse, R., Anand, M., Gattacceca, J., Joy, K.H., Mortimer, J.I., Pernet-Fisher, J.F., Russell, S., Snape, J.F., Weiss, B.P., 2019. Constraining the evolutionary history of the Moon and the inner solar system: a case for new returned lunar samples. Space Sci. Rev. 215, 54. https://doi.org/10.1007/s11214-019-0622-x.

Terada, K., Morota, T., Kato, M., 2020. Asteroid shower on the Earth-Moon system immediately before the Cryogenian period revealed by KAGUYA. Nat. Commun. 11, 3453. https://doi.org/10.1038/s41467-020-17115-6.

van der Bogert, C.H., Hiesinger, H., 2020. Which samples are needed for improved calibration of the lunar cratering chronology? In: 51st Lunar and Planetary Science Conference. Lunar and Planetary Institute, The Woodlands, Texas. Abstract #2088.

Wang, J., Zhang, Y., Di, K., Chen, M., Duan, J., Kong, J., Xie, J., Liu, Z., Wan, W., Rong, Z., Liu, B., Peng, M., Wang, Y., 2021. Localization of the Chang'e-5 lander using radio-tracking and image-based methods. Remote Sens. https://doi.org/10.3390/rs13040590.

Watters, T.R., 1988. Wrinkle ridge assemblages on the terrestrial planets. J. Geophys. Res., Solid Earth 93, 10236–10254. https://doi.org/10.1029/JB093iB09p10236.

Watters, T.R., Robinson, M.S., Banks, M.E., Tran, T., Denevi, B.W., 2012. Recent extensional tectonics on the Moon revealed by the Lunar Reconnaissance Orbiter Camera. Nat. Geosci. 5, 181. https://doi.org/10.1038/ngeo1387. https://www.nature.com/articles/ngeo1387#supplementary-information.

Wilson, L., Head, J.W., 2018. Controls on lunar basaltic volcanic eruption structure and morphology: gas release patterns in sequential eruption phases. Geophys. Res. Lett. 45. https://doi.org/10.1029/2018GL078327.

Wilson, L., Head, J.W., 2017. Generation, ascent and eruption of magma on the Moon: new insights into source depths, magma supply, intrusions and effusive/explosive eruptions (Part 1: theory). Icarus 283, 146–175. https://doi.org/10.1016/j.icarus.2015.12.039.

Wu, B., Huang, J., Li, Y., Wang, Y., Peng, J., 2018. Rock abundance and crater density in the candidate Chang'E-5 landing region on the Moon. J. Geophys. Res., Planets 123, 3256–3272. https://doi.org/10.1029/2018JE005820.

Xiao, L., Zhu, P., Fang, G., Xiao, Z., Zou, Y., Zhao, J., Zhao, N., Yuan, Y., Qiao, L., Zhang, X., Zhang, H., Wang, J., Huang, J., Huang, Q., He, Q., Zhou, B., Ji, Y., Zhang, Q., Shen, S., Li, Y., Gao, Y., 2015. A young multilayered terrane of the northern Mare Imbrium revealed by Chang'E-3 mission. Science 347, 1226. https://doi.org/10.1126/science.1259866.

Xiao, Z., 2018. On the importance of self-secondaries. Geosci. Lett. 5, 17. https://doi.org/10.1186/s40562-018-0116-9.

Xie, M., Xiao, Z., Zhang, X., Xu, A., 2020. The provenance of regolith at the Chang'e-5 candidate landing region. J. Geophys. Res., Planets 125, e2019JE006112. https://doi.org/10.1029/2019JE006112.

Yue, Z., Michael, G.G., Di, K., Liu, J., 2017. Global survey of lunar wrinkle ridge formation times. Earth Planet. Sci. Lett. 477, 14–20. https://doi.org/10.1016/j.epsl.2017.07.048.

Zanetti, M., Stadermann, A., Jolliff, B., Hiesinger, H., van der Bogert, C.H., Plescia, J., 2017. Evidence for self-secondary cratering of Copernican-age continuous ejecta deposits on the Moon. Icarus 298, 64–77. https://doi.org/10.1016/j.icarus.2017.01.030.

Zhang, G.L., Li, C.L., Liu, D.W., Liu, B., Zhou, Q., Gao, F., Zhang, H.B., Kong, D.Q., Ren, X., 2020. Storage, processing, and preparation methods for China's returned lunar samples. In: 51st Lunar Planet. Sci. Conf.

Zhang, J.Y., Head, J.W., Liu, J.Z., Potter, R.W.K., 2021. Analysis of thorium concentration anomalies on the lunar surface. In: 52nd Lunar and Planetary Science Conference. Abstract #1744.

Zhao, J., Huang, J., Qiao, L., Xiao, Z., Huang, Q., Wang, J., He, Q., Xiao, L., 2014. Geologic characteristics of the Chang'E-3 exploration region. Sci. China, Phys. Mech. Astron. 57, 569–576. https://doi.org/10.1007/s11433-014-5399-z.

Zhao, J., Xiao, L., Qiao, L., Glotch, T.D., Huang, Q., 2017. The Mons Rümker volcanic complex of the Moon: a candidate landing site for the Chang'E-5 mission. J. Geophys. Res., Planets 122, 1419–1442. https://doi.org/10.1002/2016JE005247.